Many-body theory of chemotactic cell-cell interactions

T. J. Newman[1,2] and R. Grima[1]
[1]*Department of Physics and Astronomy, Arizona State University, Tempe, Arizona 85284, USA*
[2]*School of Life Sciences, Arizona State University, Tempe, Arizona 85284, USA*
(Received 4 June 2004; published 29 November 2004)

We consider an individual-based stochastic model of cell movement mediated by chemical signaling fields. This model is formulated using Langevin dynamics, which allows an analytic study using methods from statistical and many-body physics. In particular we construct a diagrammatic framework within which to study cell-cell interactions. In the mean-field limit, where statistical correlations between cells are neglected, we recover the deterministic Keller-Segel equations. Within exact perturbation theory in the chemotactic coupling ϵ, statistical correlations are non-negligible at large times and lead to a renormalization of the cell diffusion coefficient D_R—an effect that is absent at mean-field level. An alternative closure scheme, based on the necklace approximation, probes the strong coupling behavior of the system and predicts that D_R is renormalized to zero at a critical value of ϵ, indicating self-localization of the cell. Stochastic simulations of the model give very satisfactory agreement with the perturbative result. At higher values of the coupling simulations indicate that $D_R \sim \epsilon^{-2}$, a result at odds with the necklace approximation. We briefly discuss an extension of our model, which incorporates the effects of short-range interactions such as cell-cell adhesion.

DOI: 10.1103/PhysRevE.70.051916 PACS number(s): 87.17.−d, 87.18.−h, 05.10.Gg

I. INTRODUCTION

Cell movement via chemotaxis is a fundamental process in both unicellular and multicellular organisms [1]. Chemotaxis is broadly defined as movement in response to a chemical gradient. Microorganisms use chemotaxis to locate food sources, avoid obstacles, and in some cases to aggregate with like cells to form fruiting bodies [2,3]. Such aggregating cellular systems have been of intense theoretical interest for many years, and have typically been modeled using coupled differential equations, most notably the Keller-Segel (KS) model and its variants [4–7]. More recently theoretical attention has been focused on other, more complex, forms of chemotaxis, typically in higher organisms; examples being intercellular organization in the early embryo [8–10], and the use of chemotaxis for specific location of targets, such as leucocytes locating bacteria [11] and sperm locating ova [12].

From a statistical physics viewpoint it is natural to investigate the role of fluctuations during chemotaxis in multicellular systems. The KS model and its variants have the form of mean-field type models and, according to the conventional wisdom from critical phenomena, will not be able to address such questions [13]. Some groups have been probing fluctuations implicitly by constructing computer algorithms of cell movement and cell interactions; in particular, we mention the work of Drasdo *et al.* [14–16], who have developed Monte Carlo simulations for a range of multicellular processes (e.g., tumor growth and wound healing), and Glazier *et al.*, who have used an ingenious form of the Potts model (in which a given spin orientation identifies a unique cell) to model a variety of cellular systems [17–19].

In this paper we address the question of chemotactic fluctuations from an analytic viewpoint by introducing a stochastic model of cell movement which is amenable to calculation. A quantitative understanding of fluctuations in cell-cell interactions is necessary in order to uncover the constraints within which the evolution of multicellularity has proceeded. The biological insight afforded by such an understanding is the long-term goal of this work. In this introductory paper we aim to present a comprehensible theoretical description of our model and its preliminary analysis.

The outline of the paper is as follows. In the next section we define the model, which is written in terms of Langevin dynamics. We show that the equations of motion for probability distributions have an infinite hierarchy. In Sec. III we construct a diagrammatic representation of this hierarchy which greatly simplifies both analysis and interpretation of statistical fluctuations. In Sec. IV we enforce a mean-field truncation of the model. We show that the resulting model corresponds precisely to the KS equations, which provides a useful benchmark for our theory. In Sec. V we proceed to account for fluctuations systematically within perturbation theory—this is conveniently handled using diagrammatic methods. We present results to second order, and show that fluctuations (via cell-cell correlations) lead to a renormalization of the cell diffusion constant. In Sec. VI we go beyond perturbation theory using the simplest approximate resummation of the diagrams—namely, the necklace (or Hartree-Fock) approximation. This scheme predicts both a renormalization of the diffusion constant and, for larger couplings, a self-localization transition. We test these predictions, in Sec. VII, by means of a careful numerical simulation of the model in one dimension. The perturbative results are quantitatively confirmed, but the self-localization transition is not observed. We emphasize that our numerical algorithm is very efficient in describing large numbers of cells in higher dimensions, since the algorithm does not require an underlying grid and its speed is thus relatively insensitive to the dimensionality of space. Then, in Sec. VIII, we briefly discuss some extensions of our model which are necessary to describe short-range adhesive interactions between cells. We summarize our results and discuss future work in Sec. IX.

II. THE BASIC MODEL

As mentioned in the Introduction, we are interested in the statistical correlations between cells which share a chemical signaling field. The simplest way to investigate this is to construct a model in which the cells, perforce, are described on an individual basis, but in which the chemical signals are treated in the continuum limit. For all but the lowest chemical concentrations, this appears to be a reasonable length-scale separation to make.

We consider N identical cells moving in a d-dimensional space. The position of cell i is denoted by $\mathbf{x}_i$. Each cell emits a chemical signal with rate β, and chemotactically responds to the gradient of the chemical field with constant chemotactic susceptibility α. The concentration of the chemical field is denoted by $\phi(\mathbf{x},t)$. The molecules comprising the chemical field have diffusion constant D_1 and a degradation rate λ. In the absence of the chemical field, the cells perform pure random walks with diffusion constant D_0. This process of emitting and responding to chemical signals will encourage aggregation for $\alpha>0$ ("positive chemotaxis") and mutual repulsion for $\alpha<0$ ("negative chemotaxis"). Although we place no restriction on the sign of α we will generally have in mind $\alpha>0$ since this allows us to compare our results to the well-studied case of cell aggregation.

Our model can be written down mathematically in the form of a Langevin equation [20]. We have for the cells

$$\dot{\mathbf{x}}_i = \xi_i + \alpha \boldsymbol{\nabla}_i \phi, \tag{1}$$

where the gradient of ϕ is evaluated at the current position of cell i. The noise ξ_i is responsible for the random walk aspect of the cell's dynamics, and for simplicity is sampled from a Gaussian distribution with zero mean and correlator

$$\langle \xi_i^a(t) \xi_j^b(t') \rangle = 2D_0 \delta_{a,b} \delta_{i,j} \delta(t-t'), \tag{2}$$

where a and b refer to spatial components of the noise vectors. The chemical concentration field is modeled by a diffusion equation of the form

$$\partial_t \phi = D_1 \nabla^2 \phi - \lambda \phi + \beta \sum_{i=1}^{N} \delta(\mathbf{x} - \mathbf{x}_i(t)). \tag{3}$$

A similar model in which both the cells and the chemical molecules are treated as discrete entities has been proposed by Stevens [21]. This model formulation is easily extended to accommodate multiple signaling fields and cell types. Regarding the latter, one can introduce different cell phenotypes by allowing parameters such as α, β, and D_0 to depend on the cell index i. We refer the reader to Fig. 1 for a schematic representation of chemical signaling between different cell types. For simplicity we assume a population of identical cells in the remainder of this paper.

The Langevin formulation for cell dynamics given above is attractive in that it allows intuitive model building, since one is considering equations of motion for each cell. Furthermore, it allows optimized computer algorithms to be constructed (see Sec. VII). The Langevin formulation is not, however, the most convenient representation of the model for the purposes of analytic calculations. In this case one can proceed more easily by deriving differential equations for the single-cell and multicell probability distributions.

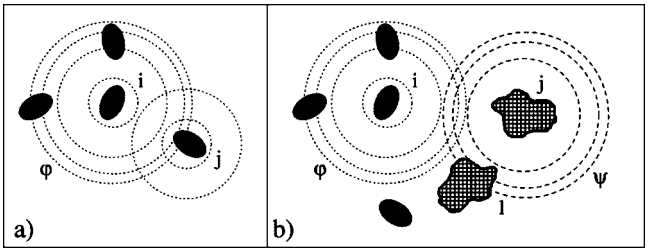

FIG. 1. Schematic diagram of cell-cell interactions. In (a) cells of one type release and respond to a chemoattractant denoted by ϕ. Cells i and j could, for instance, represent myxobacteria. In (b) we illustrate a more complex scenario of two cell types interacting via chemical signals, with concentration fields denoted by ϕ and ψ. Cells i and j could, for instance, represent a bacterium (i) attempting to evade predation by an amoeba (j), with field ϕ representing a chemoattractant secreted inadvertently by the bacteria (allowing the amoeba to locate them), and ψ representing a mutual chemorepulsive signal between amoebas (j and l) allowing them to feed efficiently. The calculations in the present paper will be restricted to a single cell type (a), although the many-body formulation is able to accommodate multiple cell types and multiple signaling fields.

We define the single-cell probability distribution via

$$P_i(\mathbf{x},t) = \langle \delta(\mathbf{x} - \mathbf{x}_i(t)) \rangle, \tag{4}$$

where the angled brackets indicate an average over the noise. In a similar manner one defines the multicell distributions, e.g., the two-cell probability distribution

$$P_{i,j}(\mathbf{x},t;\mathbf{x}',t') = \langle \delta(\mathbf{x} - \mathbf{x}_i(t)) \delta(\mathbf{x}' - \mathbf{x}_j(t')) \rangle. \tag{5}$$

In order to find an equation of motion for P_i we first express the concentration field ϕ in terms of the cell paths. This is accomplished by formally integrating Eq. (3), the result being

$$\phi(\mathbf{x},t) = \beta \int d^d x' \int_0^t dt' G_\lambda(\mathbf{x} - \mathbf{x}', t - t') \sum_j \delta(\mathbf{x}' - \mathbf{x}_j(t')), \tag{6}$$

where we have defined the Green function for the chemical diffusion equation,

$$G_\lambda(\mathbf{x},t) = (4\pi D_1 t)^{-d/2} \exp\left[-\frac{x^2}{4D_1 t} - \lambda t \right]. \tag{7}$$

We have imposed an initial condition of zero concentration field. This choice is made on the grounds of simplicity. As a technical point, it is helpful to leave the δ function intact in Eq. (6).

We now consider the time derivative of P_i. From the definition (4) above we have

$$\begin{aligned} \partial_t P_i(\mathbf{x},t) &= -\boldsymbol{\nabla} \cdot \langle \dot{\mathbf{x}}_i(t) \delta(\mathbf{x} - \mathbf{x}_i(t)) \rangle \\ &= -\boldsymbol{\nabla} \cdot \langle \xi_i \delta(\mathbf{x} - \mathbf{x}_i(t)) \rangle - \alpha \boldsymbol{\nabla} \cdot \langle \boldsymbol{\nabla}_i \phi \delta(\mathbf{x} - \mathbf{x}_i(t)) \rangle. \end{aligned} \tag{8}$$

The first term on the right-hand side of Eq. (8) is the standard term that appears in deriving the Fokker-Planck equation for a pure random walk and is not affected by the presence of the chemical field. It can be evaluated by standard methods [20] to give a term proportional to the Laplacian of P_i. The second term may be evaluated by inserting the formal solution (6) and rewriting the average over δ functions in terms of the two-cell distribution function (5). One then has

$$\partial_t P_i = D_0 \nabla^2 P_i - \epsilon \nabla \cdot \int d^d x' \int_0^t dt' [\nabla G_\lambda(\mathbf{x}-\mathbf{x}', t-t')] \times \sum_j P_{i,j}(\mathbf{x}, t; \mathbf{x}', t'), \tag{9}$$

where we have introduced the "chemotactic coupling" $\epsilon = \alpha\beta$.

The chemical field introduces statistical correlations between the cells (via the Green function G_λ). Thus, the one-cell distribution function requires knowledge of the two-cell distribution. Naturally, the equation of motion for the two-cell distribution will involve the three-cell distribution and so on, yielding an infinite hierarchy of distribution functions typical of interacting many-body systems [22]. Note that even for a single cell there will be nontrivial statistical correlations (contained within $P_{i,i}$) due to past fluctuations of the cell being mediated through the chemical field and affecting the same cell at future times. We shall see that such autochemotactic effects play an important role in the long-time dynamics of the system.

III. STATISTICAL CORRELATIONS AND DIAGRAMMATICS

Given the complex structure of the hierarchy of distribution functions, it is desirable to represent the theory in terms of diagrams. This allows a compact means by which to express the theory, and also aids interpretation of the statistical correlations which are central to the cell dynamics. We refer the reader to Appendix A for a brief overview of the diagrammatic techniques used in this paper.

As is typically the case with many-body theories, it is convenient to develop a diagrammatic representation in Fourier space. Thus we introduce the Fourier transforms

$$\tilde{P}_i(\mathbf{k}, t) = \int d^d x \, P_i(\mathbf{x}, t) e^{i\mathbf{k}\cdot\mathbf{x}} \tag{10}$$

and

$$\tilde{P}_{i,j}(\mathbf{k}, t; \mathbf{k}', t') = \int d^d x \, d^d x' \, P_{i,j}(\mathbf{x}, t; \mathbf{x}', t') e^{i\mathbf{k}\cdot\mathbf{x} + i\mathbf{k}'\cdot\mathbf{x}'}. \tag{11}$$

On taking the Fourier transform of Eq. (9) we find

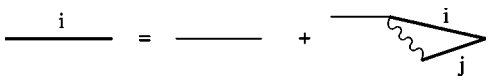

FIG. 2. Diagrammatic representation of Eq. (13): the single-cell distribution $\tilde{P}_i$ in terms of the two-cell distribution $\tilde{P}_{i,j}$.

$$\partial_t \tilde{P}_i(\mathbf{k}, t) = -D_0 k^2 \tilde{P}_i(\mathbf{k}, t) + \epsilon \int_0^t dt' \int dk' (\mathbf{k}\cdot\mathbf{k}') \times \tilde{G}_\lambda(\mathbf{k}', t-t') \sum_j \tilde{P}_{i,j}(\mathbf{k}-\mathbf{k}', t; \mathbf{k}', t'), \tag{12}$$

where dk is shorthand for the wave vector volume element $d^d k/(2\pi)^d$.

We have yet to discuss the initial condition for the cells. In this paper we choose perhaps the simplest, namely, that the cells are all initially confined to some small region. We therefore take $P_i(\mathbf{x}, 0) = \delta(\mathbf{x})$ which corresponds to $\tilde{P}_i(\mathbf{k}, 0) = 1$. As time proceeds, the cells will attempt diffusion, which will be, to some degree, balanced by chemotactic confinement of the cells (for $\epsilon > 0$) due to their production of the chemical field. Many other initial conditions are of course possible depending on the particular biological conditions of interest. It is sometimes convenient to consider random initial conditions (RIC), since these allow a convenient definition of cell propagators. We shall not explicitly consider RIC here, but they are easily included in the diagrammatic expansion described below.

Equation (12) may now be integrated forward in time to give

$$\tilde{P}_i(\mathbf{k}, t) = \tilde{G}_0(\mathbf{k}, t) + \epsilon \int_0^t dt' \tilde{G}_0(\mathbf{k}, t-t') \times \int_0^{t'} dt'' \int dk' (\mathbf{k}\cdot\mathbf{k}') \tilde{G}_\lambda(\mathbf{k}', t'-t'') \times \sum_j \tilde{P}_{i,j}(\mathbf{k}-\mathbf{k}', t'; \mathbf{k}', t''), \tag{13}$$

where we have introduced the Green function G_0, which is appropriate for a cell performing a pure random walk with diffusion constant D_0:

$$G_0(\mathbf{x}, t) = (4\pi D_0 t)^{-d/2} \exp\left[-\frac{x^2}{4 D_0 t} \right]. \tag{14}$$

In Fig. 2 we represent Eq. (13) in terms of diagrams. Time flows from right to left, and each line carries a wave vector (not shown explicitly). Wave vectors are conserved at vertices due to spatial translational invariance. The heavy line with index i represents $\tilde{P}_i$, while the faint line represents the free cell propagator $\tilde{G}_0$. The Green function (or propagator) for the chemical field, $\tilde{G}_\lambda$, is represented by a wavy line. The intersection point of the wavy line with the cell propagator represents the chemotactic response and has a weight ϵ, along with an additional factor of $\mathbf{k}_1 \cdot \mathbf{k}_2$ where $\mathbf{k}_1$ and $\mathbf{k}_2$ are, respectively, the wave vectors associated with the propagator for the chemical field and the outgoing free cell propagator.

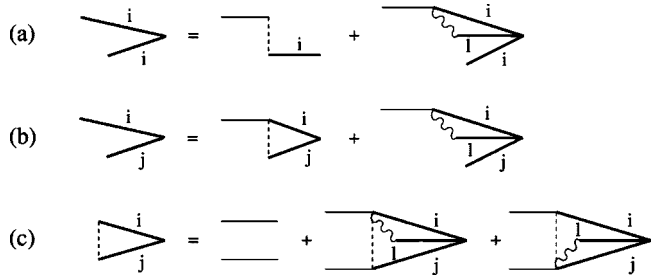

FIG. 3. Diagrammatic representations of the two-cell distribution $\tilde{P}_{i,j}(\mathbf{k},t;\mathbf{k}',t')$ for (a) $i=j$, (b) $i\neq j$ with $t>t'$, and (c) $i\neq j$ with $t=t'$. These diagrammatic equations correspond to Eqs. (15)–(17), respectively.

Finally, the "V-shaped" solid line with indices i and j represents the two-cell distribution function $\tilde{P}_{i,j}$. In order to proceed it is necessary to derive an equation of motion for this two-cell distribution function. We must be careful to distinguish between the two cases $i=j$ and $i\neq j$.

Consider first $P_{i,i}(\mathbf{x},t;\mathbf{x}',t')$, with $t>t'$. Following a procedure identical to that used in the derivation of Eq. (9), we find an equation of motion for $P_{i,i}$. We Fourier transform this equation and integrate the time variable t back to t'. This leads us to

$$\tilde{P}_{i,i}(\mathbf{k},t;\mathbf{k}',t') = \tilde{G}_0(\mathbf{k},t-t')\tilde{P}_i(\mathbf{k}+\mathbf{k}',t') + \epsilon\int_{t'}^{t} dt''\tilde{G}_0(\mathbf{k},t-t'')\int_0^{t''} dt'''\int dk''(\mathbf{k}\cdot\mathbf{k}'') \times\tilde{G}_\lambda(\mathbf{k}'',t''-t''') \times\sum_l \tilde{P}_{i,i,l}(\mathbf{k}-\mathbf{k}'',t'';\mathbf{k}',t';\mathbf{k}'',t'''). \quad (15)$$

This equation is illustrated diagrammatically in Fig. 3(a). The dashed line is simply a bookkeeping device fixing its two ends at identical times (in this case t'). Note, the internal time t''' may be less than or greater than the external time t', but both are strictly less than the internal time t''. The careful treatment of causality such as this is crucial for generating correct diagrams in perturbation theory, as we shall see in Sec. V.

We now turn to $P_{i,j}(\mathbf{x},t;\mathbf{x}',t')$ with $i\neq j$ and $t>t'$. Following an analogous procedure to that used for $P_{i,i}$ we arrive at the equation

FIG. 4. The diagrammatic analog of Fig. 2 under the mean-field approximation—the two-cell distribution is expressed as the product of two one-cell distributions. Iteration of this equation yields an infinite set of tree-level diagrams.

$$\tilde{P}_{i,j}(\mathbf{k},t;\mathbf{k}',t') = \tilde{G}_0(\mathbf{k},t-t')\tilde{P}_{i,j}(\mathbf{k},t';\mathbf{k}',t') + \epsilon\int_{t'}^{t} dt''\tilde{G}_0(\mathbf{k},t-t'')\int_0^{t''} dt'''\int dk''(\mathbf{k}\cdot\mathbf{k}'') \times\tilde{G}_\lambda(\mathbf{k}'',t''-t''') \times\sum_l \tilde{P}_{i,j,l}(\mathbf{k}-\mathbf{k}'',t'';\mathbf{k}',t';\mathbf{k}'',t'''). \quad (16)$$

This equation is illustrated diagrammatically in Fig. 3(b). We must treat one more two-cell distribution, namely, the equal-time function $P_{i,j}(\mathbf{x},t;\mathbf{x}',t)$ with $i\neq j$. The same procedure as outlined above (with the time t integrated back to the initial time zero) yields

$$\tilde{P}_{i,j}(\mathbf{k},t;\mathbf{k}',t) = \tilde{G}_0(\mathbf{k},t)\tilde{G}_0(\mathbf{k}',t) + \epsilon\int_0^{t} dt'\tilde{G}_0(\mathbf{k},t-t') \times\tilde{G}_0(\mathbf{k}',t-t')\int_0^{t'} dt''\int dk''(\mathbf{k}\cdot\mathbf{k}'')\tilde{G}_\lambda \times\sum_l [\tilde{P}_{i,j,l}(\mathbf{k}-\mathbf{k}'',t';\mathbf{k}',t';\mathbf{k}'',t'') + \tilde{P}_{i,j,l}(\mathbf{k},t';\mathbf{k}'-\mathbf{k}'',t';\mathbf{k}'',t'')]. \quad (17)$$

This equation is illustrated diagrammatically in Fig. 3(c).

The diagrammatic relations in Figs. 3(a)–3(c) are exact and encapsulate the two-cell interactions in terms of three-cell interactions. It is relatively straightforward to express these three-cell interactions in terms of higher-order processes. Care must be taken to distinguish cases of coincident cell indices, and coincident times. We shall not pursue this here. The relations in Fig. 3 are sufficient to yield useful insight into statistical correlations, and to generate perturbative corrections to P_i up to and including second order in the chemotactic coupling ϵ. Before proceeding with such an analysis, let us first gain some intuition by studying the system from a mean-field perspective.

IV. THE DETERMINISTIC LIMIT

Past models of chemotaxis have typically been formulated in terms of nonlinear coupled partial differential equations (written in terms of the cell density and chemical concentration), based on deterministic dynamics; the canonical example being the well-known KS equations [4,5]. Here, we shall attempt to make contact with such models by imposing a mean-field approximation on our model, at the level of Eq. (9).

The two-cell distribution function can be exactly rewritten in terms of a conditional probability distribution, viz.,

$$P_{i,j}(\mathbf{x},t;\mathbf{x}',t') = P_{i|j}(\mathbf{x},t|\mathbf{x}',t')P_j(\mathbf{x}',t'). \quad (18)$$

The mean-field approximation may now be stated clearly as

$$P_{i|j}(\mathbf{x},t|\mathbf{x}',t') = P_i(\mathbf{x},t) \quad \forall \quad j, \quad (19)$$

namely, we assume that the probability of finding cell i at position $\mathbf{x}$ at time t is statistically independent of the previous positions of all the cells.

Then from (18), $P_{i,j}=P_iP_j$ and it is a simple matter to rewrite Eq. (9) in the form

$$\partial_t P_i = D_0\nabla^2 P_i - \epsilon\,\boldsymbol{\nabla}\cdot P_i(\mathbf{x},t)\,\boldsymbol{\nabla}\int d^dx'\int_0^t dt' \times G_\lambda(\mathbf{x}-\mathbf{x}',t-t')\sum_j P_j(\mathbf{x}',t'). \quad (20)$$

This equation (in Fourier space and integrated forward in time) is represented diagrammatically in Fig. 4. The equation for P_i is self-consistent, and on iteration will yield "tree diagrams."

We now show that Eq. (20) is identical to the KS equations. First we define the density of cells via

$$\rho(\mathbf{x},t)=\sum_i P_i(\mathbf{x},t). \quad (21)$$

Summing Eq. (20) over the cell index we obtain a partial differential equation for the density:

$$\partial_t\rho = D_0\nabla^2\rho - \alpha\,\boldsymbol{\nabla}\cdot\rho\,\boldsymbol{\nabla}\Phi, \quad (22)$$

where the ensemble averaged chemical field $\Phi(\mathbf{x},t)$ is defined via

$$\Phi(\mathbf{x},t)=\beta\int d^dx'\int_0^t dt' G_\lambda(\mathbf{x}-\mathbf{x}',t-t')\rho(\mathbf{x}',t') \quad (23)$$

(we remind the reader that $\epsilon=\alpha\beta$). Given the definition of the Green function G_λ it is clear that Φ satisfies the partial differential equation

$$\partial_t\Phi = D_1\nabla^2\Phi - \lambda\Phi + \beta\rho. \quad (24)$$

The coupled equations (22) and (24) for the cell density and chemical concentration are identical to the KS equations. The KS equations have previously been rigorously derived, for a range of coupling strengths, from a stochastic model similar to ours, in which both the cells and the chemical signaling molecules are described in a discrete fashion. The derivation relies on the limit of infinite number of particles to be taken [21]. The derivation given here is complementary to this in that it highlights how the KS equations arise from a mean-field approximation in which statistical correlations between cells are neglected.

V. PERTURBATION THEORY

The mean-field truncation given in Eq. (19) is an uncontrolled approximation. It is desirable to probe the importance of fluctuations in a systematic manner. In this section we shall develop an exact treatment of statistical correlations between cells within a perturbative scheme. Our perturbative parameter will be the chemotactic coupling ϵ, which is proportional to both the strength of response of the cells to the chemical field, and to the rate of production of the chemical.

With the aid of the exact diagrammatic relations in Fig. 3 we can generate a perturbative expansion for $\tilde{P}_i(\mathbf{k},t)$ to second order in ϵ. This is achieved by replacing all three-cell diagrams by their zeroth-order form (corresponding to a system of N noninteracting cells performing random walks). The only subtlety relates to coincident cell indices, and subsequent time ordering. Due to this, the three-cell diagram can take several different forms, which are shown in Fig. 5. Again, the dashed lines are simply a bookkeeping device reminding us that the ends of a given dashed line are to be taken at equal times. We shall typically contract the dashed lines, in the loop expansion, for a more compact representation.

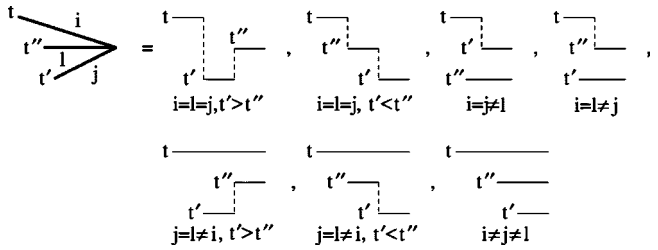

FIG. 5. The possible zeroth-order forms for $\tilde{P}_{i,j,l}(\mathbf{k},t;\mathbf{k}',t';\mathbf{k}'',t'')$.

On iterating the single-cell equation in Fig. 2 with the aid of the two-cell equations in Fig. 3 we can insert the zeroth-order three-cell terms from Fig. 5 where appropriate to generate a perturbative series up to and including second order in ϵ. Two diagrams appear at first order, and 12 diagrams at second order. These are illustrated in Fig. 6.

The diagrams can be classified in different groups: (i) tree diagrams, (ii) diagrams which renormalize the cell propagator, (iii) diagrams which renormalize the chemotactic response, (iv) diagrams corresponding to new, higher-order nonlinear processes, and (v) diagrams which, through iteration, arise from groups (i)–(iv). Referring to Fig. 6, the one-loop diagrams *a* and *b* are in classes (i) and (ii), respectively. Of the 12 two-loop diagrams, *c*, *d*, and *e* are in class (v); *f* and *g* are in class (i); *h*, *i*, and *j* are in class (ii); *k*, *l*, and *m* are in class (iii); and finally, diagram *n* is in class (iv), and

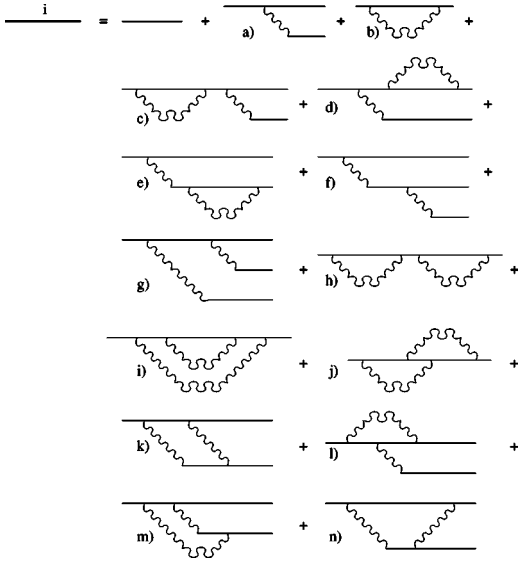

FIG. 6. Diagrams contributing to $\tilde{P}_i(\mathbf{k})$ up to and including second order in ϵ.

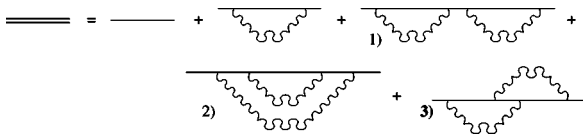

FIG. 7. Diagrams contributing to the renormalization of the cell propagator, up to and including second order in ϵ. The two-loop diagrams (1), (2), and (3) are referred to in the main text as the "necklace," "rainbow," and "crossover" diagrams, respectively.

represents a new interaction in which "autoresponse" is mediated via a second cell. Many of these diagrams are familiar from the study of interacting Fermi systems [23,24].

In this section, we shall focus on the second class of diagrams and investigate the effects of statistical fluctuations on the "renormalization" of the diffusion constant for a given cell. In Fig. 7 we show those diagrams which renormalize the cell propagator, which we denote by a double line and the symbol G_R. The single-cell propagator is most easily defined by generalizing to random initial conditions. One writes

$$\tilde{G}_R(\mathbf{k},t) = \left[\frac{\delta \tilde{P}_i(\mathbf{k},t)}{\delta \tilde{P}_i(\mathbf{k},0)} \right]_{\mathrm{IC}}, \tag{25}$$

where the square brackets indicate an average over the ensemble of random uncorrelated initial cell positions. Diagrammatically one can represent the random cell position by a cross which terminates each cell propagator at $t=0$. By differentiating with respect to $\tilde{P}_i(\mathbf{k},0)$ and averaging, it is easy to see that we retain only those diagrams which renormalize the cell propagator. (This propagator is precisely equal to $\tilde{P}_i$ for the case of a system containing only one cell with the initial conditions specified earlier, and in which the only interactions are autochemotactic.) We shall describe the evaluation of the single one-loop diagram in Fig. 7 in some detail. Technical details relating to the (rather more difficult) evaluation of the two-loop diagrams can be found in Appendix B, and are restricted to the case of $d=1$.

We write

$$\tilde{G}_R(\mathbf{k},t) = \tilde{G}_R^{(0)}(\mathbf{k},t) + \epsilon \tilde{G}_R^{(1)}(\mathbf{k},t) + \epsilon^2 \tilde{G}_R^{(2)}(\mathbf{k},t) + O(\epsilon^3), \tag{26}$$

where $\tilde{G}_R^{(0)} = \tilde{G}_0 = \exp(-D_0 k^2 t)$. The one-loop diagram in Fig. 7 provides the contribution

$$\tilde{G}_R^{(1)}(\mathbf{k},t) = \int_0^t dt' \int_0^{t'} dt'' \int d k_1 \mathbf{k}\cdot\mathbf{k}_1 \tilde{G}_0(\mathbf{k},t-t') \times \tilde{G}_0(\mathbf{k}-\mathbf{k}_1,t'-t'') \tilde{G}_\lambda(\mathbf{k}_1,t'-t'') \tilde{G}_0(\mathbf{k},t''). \tag{27}$$

It turns out that so long as $\lambda > 0$ the perturbative corrections to $\tilde{G}_R$ are finite in the long-time regime and serve to renormalize the propagator. We shall quantify this by studying the renormalization of the diffusion constant. There are also corrections which distort the Gaussian nature of the propagator, but we do not consider these here. For the case $\lambda = 0$ in low dimensions ($d \leqslant 2$), the perturbative corrections are not small in the long-time regime signaling a qualitative change of behavior away from diffusion. Here we exclusively focus on $\lambda > 0$, which is the case of most biological relevance.

It is most straightforward to study renormalization of the diffusion constant by the following construction. First, we Laplace transform in time, i.e.,

$$\hat{G}_R(\mathbf{k},s) \equiv \mathcal{L}_{s|t}[\tilde{G}_R(\mathbf{k},t)] = \int_0^\infty dt\, e^{-st} \tilde{G}_R(\mathbf{k},t). \tag{28}$$

Then at leading order we have

$$\hat{G}_R^0(\mathbf{k},s) = (s + D_0 k^2)^{-1}. \tag{29}$$

Defining the renormalized diffusion constant via the property that $\langle x^2 \rangle_{P_i} = 2dD_R t$ for large times, we have

$$D_R \equiv \lim_{t\to\infty} \frac{1}{2dt} \int d^d x\, x^2 P_i(\mathbf{x},t). \tag{30}$$

It is straightforward to show from Eq. (30) that an equivalent definition is

$$D_R \equiv -\frac{1}{2d} \lim_{s\to 0} s^2 [\nabla_k^2 \hat{G}_R(\mathbf{k},s)]_{\mathbf{k}=0}. \tag{31}$$

It is convenient to introduce the notation corresponding to Eq. (26):

$$D_R = D_R^{(0)} + \epsilon D_R^{(1)} + \epsilon^2 D_R^{(2)} + O(\epsilon^3), \tag{32}$$

where, naturally, $D_R^{(0)} = D_0$.

To proceed, we Laplace transform Eq. (27), and after invoking the convolution theorem (or Faltung theorem [25]) we have

$$\hat{G}_R^{(1)}(\mathbf{k},s) = \hat{G}_0(\mathbf{k},s)^2 \int d k_1 \mathbf{k}\cdot\mathbf{k}_1 \mathcal{L}_{s|t}[\tilde{G}_0(\mathbf{k}-\mathbf{k}_1,t)\tilde{G}_\lambda(\mathbf{k}_1,t)] = \hat{G}_0(\mathbf{k},s)^2 \int d k_1 \frac{\mathbf{k}\cdot\mathbf{k}_1}{[s+\lambda + D_1 k_1^2 + D_0(\mathbf{k}-\mathbf{k}_1)^2]}. \tag{33}$$

From the definition of the diffusion constant given in Eq. (31) we find

$$D_R^{(1)} = -\frac{2D_0}{d} \int d k_1 \frac{k_1^2}{[\lambda + (D_0 + D_1) k_1^2]^2}. \tag{34}$$

This integral is finite for $d < 2$, but requires a high-wave-vector ("ultraviolet") cutoff Λ for $d \geqslant 2$. This uv cutoff corresponds to a short-distance cutoff in real space, such as the cell diameter, which is assumed to be zero in our model. We shall discuss short-range interactions between cells in more detail in Sec. VIII. On evaluating the integral in Eq. (34) we have the one-loop result:

$$D_R = D_0[1 - \epsilon_R(d) + O(\epsilon_R(d)^2)]. \tag{35}$$

The d-dependent dimensionless couplings are defined via

$$\tilde{\epsilon}(1) = \frac{\epsilon}{2\lambda^{1/2}(D_0 + D_1)^{3/2}}, \tag{36}$$

$$\tilde{\epsilon}(2) = \frac{2\pi\epsilon}{(D_0 + D_1)^2} \ln \tilde{\Lambda}, \tag{37}$$

$$\tilde{\epsilon}(3) = \frac{8\pi\epsilon\lambda^{1/2}\tilde{\Lambda}}{3(D_0 + D_1)^{5/2}}, \tag{38}$$

where

$$\tilde{\Lambda} = \left(\frac{(D_0 + D_1)}{\lambda}\right)^{1/2} \Lambda. \tag{39}$$

Thus, we see that the diffusion constant is renormalized in all dimensions to one loop in perturbation theory. The underlying process responsible for this is autochemotaxis, namely, each individual cell responding to the local chemical field in its environment produced by that particular cell. In tune with one's intuition, the renormalized diffusion constant is reduced for positive chemotactic response in which the cells are attracted to their previous emitted signal (i.e., the case $\epsilon > 0$).

It is interesting to note that the one-loop tree diagram (diagram a in Fig. 6) gives a contribution to P_i which is smaller by a factor of $(\lambda t)^{-1/2}$ and thus does not renormalize the single-cell probability distribution in the long-time regime. In other words, the mean-field theory (which corresponds to the KS model) has a long-time dynamics of pure diffusion, with $D_R = D_0$, within a perturbative treatment. This is expected to break down for strong coupling, where one finds the collapse or "blowup" phases [6].

We turn briefly to the two-loop results. The motivation for studying higher-order diagrams is to investigate whether the renormalization of the diffusion constant is still a valid concept (meaning that the second-order terms yield finite contributions for $t \to \infty$), and if so, whether the sign of the correction is positive or negative. If the latter is true, this may indicate a collapse transition, in which D_R becomes zero for some finite value of ϵ. We shall, in fact, find that the second-order contribution to D_R is always positive, hinting that the collapse transition may not occur at all for the discrete cell system. We restrict our analysis of the two-loop corrections to $d = 1$, and so we use the shorthand $\tilde{\epsilon} = \tilde{\epsilon}(1)$. The dimension $d = 1$ is that in which fluctuations play the strongest role, and so, from the point of view of deviations from mean-field theory, is expected to be the most interesting case.

There are three two-loop diagrams which can renormalize D_R, as illustrated in Fig. 7. The calculation of their individual contributions is presented in Appendix B. The "necklace" diagram yields precisely zero contribution, the "rainbow" diagram yields a contribution which is either positive or negative according to the relative sizes of D_0 and D_1, and the "crossover" diagram yields a contribution which is always positive. Interestingly, the sum of the three is always positive, vanishing precisely in the limit of $D_1 \to 0$. On defining the relative diffusion constant

$$\delta \equiv \frac{D_0}{D_0 + D_1}, \tag{40}$$

we have

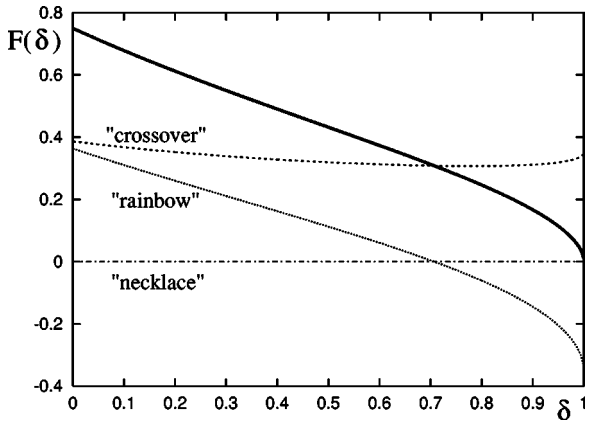

FIG. 8. The two-loop contribution to the renormalized diffusion coefficient $F(\delta)$ vs $\delta = D_0/(D_0 + D_1)$ (solid line). The dashed lines show the individual contributions from the three two-loop diagrams (see Appendix B).

$$D_R = D_0[1 - \tilde{\epsilon} + F(\delta)\tilde{\epsilon}^2 + O(\tilde{\epsilon}^3)]. \tag{41}$$

The two-loop coefficient is given by

$$F(\delta) = \frac{(1-\delta)}{\pi}\left\{\frac{(2\delta^4 + 7\delta^2 - 1)}{(1-\delta^2)^{1/2}(1+\delta^2)^2} + \frac{2(2-\delta^2)}{(1+\delta^2)^{5/2}} \sin^{-1}\left(\frac{1+\delta^2}{2}\right)^{1/2} + \frac{\pi}{2\delta^2}\left[\frac{4}{\pi(1+\delta^2)^{1/2}} \sin^{-1}\left(\frac{1+\delta^2}{2}\right)^{1/2} - 1\right]\right\}. \tag{42}$$

This function, along with its individual contributions, is plotted in Fig. 8. We give here some limiting cases:

$$F(\delta) \sim \left[\frac{2(1-\delta)}{\pi^2}\right]^{1/2}, \quad \delta \to 1, \tag{43}$$

$$F(\delta) = 0.4319\ldots, \quad \delta = 1/2, \tag{44}$$

$$F(\delta) = \frac{3}{4}(1-\delta) + O(\delta^2), \quad \delta \ll 1. \tag{45}$$

This ends our discussion of perturbation theory. This technique can be extended to study the renormalization of the chemotactic coupling, and this will be the subject of future work.

VI. NECKLACE APPROXIMATION

We now turn to an alternative closure scheme and contrast its predictions to both mean-field closure and the exact perturbative results obtained in the previous section. Given the intractability of interacting many-body systems, there has been a great deal of work over the years on resummation techniques [24]. One tries to identify an infinite subset of diagrams which can be exactly summed, thus leading to nonperturbative results. The catch, of course, is that there is

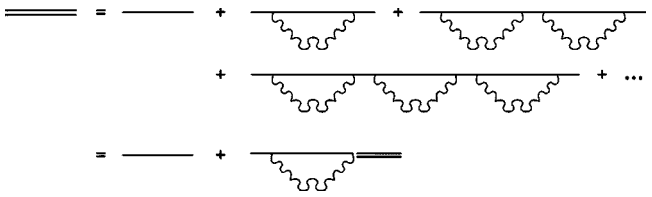

FIG. 9. Diagrammatic representation of the necklace approximation.

often no *a priori* reason why summing a particular class of diagrams is mathematically meaningful. However, it is often possible *a posteriori* to generalize the original model in such a way as to heavily weight the chosen subset of diagrams, thereby giving a limit in which the resummation is exact and allowing one to better understand the physical (or biological) basis of the nonperturbative results. These resummation techniques have proven to be an invaluable tool in nuclear and statistical physics, prime examples being the "large-n approximation" [26], the "parquet approximation" [27], and the "planar approximation" [28]. We shall examine one of the simplest such resummation schemes for our model of cell movement, namely the "necklace approximation" [29], which is akin to the Hartree-Fock approximation [24].

Referring to the diagrammatic expansion for the cell propagator (Fig. 7) we notice that the first two-loop diagram resembles a "doubled" version of the one-loop diagram. Clearly, at third order there will be a diagram with three sequential loops (or "bubbles"). If we focus on only these "bubble" or "necklace" diagrams, then we can interpret the resulting infinite perturbation expansion as a geometric series, which allows us to exactly resum all such diagrams. This strategy is illustrated diagrammatically in Fig. 9.

Although it is an unjustified approximation to keep only necklace diagrams within the current model, one can consider more complicated models for which this approximation would be reasonable. On comparing the two-loop necklace diagram to the rainbow and crossover diagrams (Fig. 7), one sees that the latter diagrams would be less important in a model which included a refractory (or "recovery") time for the cell subsequent to emitting a chemical signal. Similarly, the necklace diagrams are precisely appropriate for a model in which the cell can emit one signal only between reception events of incoming signals.

The self-consistent equation for the single-cell propagator which arises from the necklace approximation may be written as

$$\tilde{G}_R(\mathbf{k},t) = \tilde{G}_0(\mathbf{k},t) + \epsilon \int_0^t dt' \tilde{G}_0(\mathbf{k},t-t') \int_0^{t'} dt'' \int dk' \times (\mathbf{k}\cdot\mathbf{k}')\tilde{G}_\lambda(\mathbf{k}',t'-t'')\tilde{G}_0(\mathbf{k}-\mathbf{k}',t'-t'') \times \tilde{G}_R(\mathbf{k},t''). \tag{46}$$

This equation can be solved by Laplace transforming in time, and one finds

$$\hat{G}_R(\mathbf{k},s) = \frac{\hat{G}_0(\mathbf{k},s)}{1-\epsilon\hat{G}_0(\mathbf{k},s)\int dk'(\mathbf{k}\cdot\mathbf{k}')\mathcal{L}_{s|t}[\tilde{G}_\lambda(\mathbf{k}',t)\tilde{G}_0(\mathbf{k}-\mathbf{k}',t)]}. \tag{47}$$

On performing the Laplace transform of the product of the bare cell propagator and the chemical Green function one finds

$$\hat{G}_R(\mathbf{k},s) = [s + D_{\text{eff}}(\mathbf{k},s)k^2]^{-1}, \tag{48}$$

where

$$D_{\text{eff}}(\mathbf{k},s) = D_0\left\{1-\tilde{\epsilon}(d)\left[1+\frac{s}{\lambda}+\left(\frac{D_1}{D_0+D_1}\right)\frac{D_0k^2}{\lambda}\right]^{-d/2}\right\}, \tag{49}$$

with $\tilde{\epsilon}(d)$ as given in Eqs. (36)–(38).

From the definition of the renormalized diffusion coefficient given in Eq. (31) it is straightforward to show that

$$D_R = D_0[1-\tilde{\epsilon}(d)], \tag{50}$$

which is identical to the one-loop perturbative result. In other words, within the necklace approximation there are no contributions to the renormalized diffusion constant from loop diagrams higher than the first. Clearly, the renormalized diffusion constant will be zero at a critical value of the chemotactic coupling defined by $\tilde{\epsilon}_c(d)=1$. For values of the coupling larger than this critical value the renormalized diffusion constant becomes negative, indicating that the necklace approximation breaks down, and the cell density becomes infinitely peaked at a single point. This is analogous to the "blowup" phase in the KS equations [6].

Precisely at the critical point one might expect some anomalous scaling behavior. This is indeed the case. Setting $\tilde{\epsilon}(d)=1$ we have from Eq. (49)

$$D_{\text{eff}}(\mathbf{k},s) \sim \frac{dD_0}{2\lambda}\left(s+\frac{D_1}{D_0+D_1}D_0k^2\right), \tag{51}$$

where we have taken $s/\lambda \ll 1$ and $D_0k^2/\lambda \ll 1$ consistent with probing the long-time, large-distance scaling behavior of the system. Inserting this form into the propagator (48) we find $s \sim k^4$. Thus, the scaling behavior of the propagator at the critical point is given by

$$\hat{G}_R(\mathbf{k},s) = \left[s+\frac{d}{2\lambda}\frac{D_1}{D_0+D_1}(D_0k^2)^2\right]^{-1}. \tag{52}$$

This indicates a subdiffusive spreading of the single-cell distribution function with a dynamical length scale $l(t)\sim t^{1/4}$. This result holds in all dimensions.

This anomalous scaling behavior, although interesting, has a serious flaw. The single-cell distribution function, which is equivalent to the renormalized propagator, is a nonnegative quantity. However, on performing an inverse Laplace-Fourier transform of Eq. (52) we find a propagator which decays with distance in an oscillatory manner, becom-

ing negative in some regions. This indicates that the necklace approximation produces unphysical results at the critical point itself, and one must therefore view the critical scaling behavior found above with caution.

VII. NUMERICAL ANALYSIS

Numerical simulation of chemotaxis via individual-based cell signaling has proven to be a nontrivial task, even within the simple models considered in this paper. We have found strong dependence of the large-scale, long-time dynamics on microscopic details of the algorithms, such as whether the cell is constrained to move on an underlying lattice, and whether the chemical field is modeled as a continuum concentration as opposed to an ensemble of discrete diffusing molecules. A detailed survey of our numerical investigations into these issues is currently in preparation [30]. For the purposes of the current paper, we wish to compare our most robust numerical results with the predictions of the perturbation theory and necklace approximation described in Secs. V and VI. This numerical work has been confined to the simplest case of a single cell using autochemotaxis to move in one spatial dimension.

We dispense altogether with an underlying grid by basing our numerical algorithm on the Langevin equation (1) and the accompanying solution of the chemical diffusion equation (6), in which the chemical concentration field has been explicitly integrated using the Green function G_λ. On performing the spatial integral over the δ function in Eq. (6) and inserting into Eq. (1) we have (on specializing to $d=1$ and setting the index $i=1$ since we deal here with a single cell)

$$\dot{x}_1(t) = \xi(t) + \epsilon \int_0^t dt' H_\lambda(x_1(t) - x_1(t'), t - t'), \qquad (53)$$

where the function H_λ is simply the spatial derivative of G_λ:

$$H_\lambda(x,t) \equiv \partial_x G_\lambda(x,t) = -\frac{x}{4(\pi D_1^3 t^3)^{1/2}} \exp\left(-\lambda t - \frac{x^2}{4D_1 t}\right). \qquad (54)$$

Thus, we need only track the history of the cell position $x(t)$. The chemical field is not explicitly evaluated in the simulation. This algorithm is easily extended to multiple cells and higher dimensions. The CPU time scales as N for N cells (if one uses neighbor tables), and naively scales as M^2 for simulations over a temporal duration $t=M\delta t$. In fact the CPU time scales linearly with M so long as $\lambda > 0$, since the exponential decay contained with the kernel of Eq. (53) allows one to restrict the time integral to the range $t' \in (t-K/\lambda, t)$, where the parameter K is typically taken to be $K=3$. We have explicitly checked the validity of this truncated interval by comparisons with simulations in which the entire cell history is retained. Note that algorithms which explicitly integrate the chemical fields on a grid of linear size L have an associated CPU time which scales as L^d and thus become progressively less efficient for higher dimensions. This disadvantage is compounded by the more serious problem of numerical artifacts introduced by the presence of an underlying grid [30].

Numerical iteration of Eq. (53) proceeds by performing a discretized version of the time integral using the previous cell positions and thus calculating the new cell velocity. This is used to predict the new position of the cell. A given noise history $\xi(t)$ defines one realization or "sample." The dynamical fluctuations tend to be very large, and so heavy sample averaging is required to produce statistically smooth data. We have used 10^5 samples to generate the data described below. This large but finite number of samples will lead to a sampling error of approximately 1% which is consistent with the scatter of points in Figs. 10 and 11. We have not shown error bars on these figures, as the sampling error is independent of $\hat{\epsilon}$.

We have examined the long-time behavior of the cell for a wide range of values of ϵ. In the data presented here we have fixed the other parameters at the values $D_0=D_1=1.0$ and $\lambda=0.05$. The time step is chosen to be $\delta t=0.2$, which is small enough to ensure numerical stability, but not so small as to prohibit long-time simulations for the necessarily large number of samples. For all values of ϵ that we have studied the cell asymptotically performs diffusion, in the sense that its spatial variance increases linearly with time. We measure the effective diffusion coefficient by extracting the slope of the variance-time curve for large times $t \in (20, 200)$ such that transient behavior from the time scale $1/\lambda$ has died away. We have explored other values for the bare diffusion constants, and consistent behavior of effective diffusion is observed in all cases. In particular, we find an effective diffusion coefficient consistent with Eq. (55) for the case of $D_0=0.1$ and $D_1=1.0$ (note, the case $D_0 \ll D_1$ is relevant to many systems of aggregating microorganisms).

One subtlety in applying this algorithm is the apparent divergence at the upper limit of the time integral in Eq. (53). Numerically, this is handled by integrating only up to the time step before the current time. One can show that this introduces an error of $O(\delta t)$ in the estimate for the diffusion coefficient. We have explicitly calculated the propagation of this error into the first-order prediction of the renormalized diffusion constant, and we find

$$D_R = D_0[1 - \hat{\epsilon} + O(\hat{\epsilon}^2)], \qquad (55)$$

where

$$\hat{\epsilon}(\delta t) = \tilde{\epsilon}\left[1 - 2\left(\frac{\lambda \delta t}{\pi}\right)^{1/2}\right], \qquad (56)$$

with the dimensionless coupling constant $\tilde{\epsilon}=\tilde{\epsilon}(1)$ defined in Eq. (36). Naturally, the prediction of D_R for nonzero δt given in Eq. (55) agrees with our perturbative result in Eq. (35) as $\delta t \to 0$.

In Fig. 10 we plot the measured values of D_R from our simulations along with the first-order perturbation theory prediction (55). The agreement is very satisfactory. It is not a simple matter to test the second-order perturbation theory predictions since (i) the tedious integrals evaluated in Appendix B need to be reevaluated for a finite δt, and (ii) higher-precision data are required to test the second-order effects, meaning another order of magnitude of computing time. We also show the effective diffusion constant as measured from

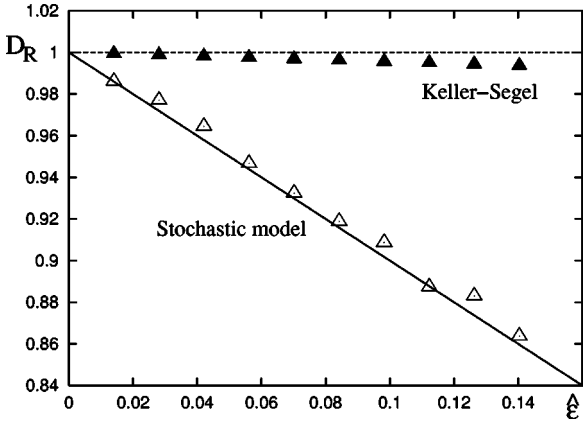

FIG. 10. Numerically measured values of the renormalized diffusion coefficient D_R versus the chemotactic coupling $\hat{\epsilon}$ [corrected for nonzero δt; cf. Eq. (56)] for a single cell (white triangles) compared to the first-order prediction of perturbation theory (55) (solid line). We also show the measured values of D_R from integration of the KS equations (black triangles) compared with the mean-field prediction (dashed line). The small disparity is due to "numerical diffusion" which results from the spatial discretization of the KS equations.

integrating the Keller-Segel equations (22) and (24). The prediction from perturbation theory is that $D_R = D_0$, within mean-field theory, since the diffusion constant is only renormalized by statistical correlations. This is borne out by the simulations. For our integration algorithm, we have used a recently developed method which has been shown to have higher precision than conventional "upwind" methods [31]. The very weak dependence of D_R on ϵ, from integrating the KS equations, is due to numerical diffusion which is an inescapable consequence of integrating advection-diffusion equations on a grid. The numerical diffusion can be made increasingly smaller by decreasing the grid size.

We have also studied the behavior of the cell variance for larger values of ϵ which lie beyond perturbation theory. We find no sign of a collapse transition in contrast to the predictions of the necklace approximation. The cell is always observed to perform effective diffusion for large times, and the renormalized diffusion constant tends to zero approximately as $D_R \sim \epsilon^{-2}$ (Fig. 11). This result is consistent with the prediction from a strong-coupling approach to auto-chemotaxis [32] based on an asymptotic analysis of the Langevin equation (1), the details of which lie beyond the scope of this paper.

VIII. SHORT-RANGE INTERACTIONS

The model as presented has treated the cells as point "particles" with no spatial extent and/or internal structure. In order to confront the model with biological reality, be it in the context of social amoeba or embryonic cell clusters, it is crucial to introduce smaller-scale interactions. Certain of these interactions are truly intracellular and require complex additional models for their description, examples being actin filament assembly to describe the details of cell motility, or signaling pathways regulating the reaction of the cell to various chemical cues [1]. Such complex mechanisms are beyond the scope, and perhaps the spirit, of the current model. Given the phenomenological nature of the model, we wish to add biological complexity in as simple a manner as possible, while maintaining biological "plausibility." Two important short-range interactions that can be described in this manner are finiteness of cell size, and cell-cell adhesion. Both may be described by introducing an effective short-ranged intercellular potential $V(|\mathbf{x}_i - \mathbf{x}_j|)$. A schematic form for V is shown in Fig. 12. The potential is characterized by two length scales: the diameter of the cell a, and the range of extension of cell-cell adhesion $b \sim 2a$. There is also an energy scale δV giving a measure of the strength of adhesion.

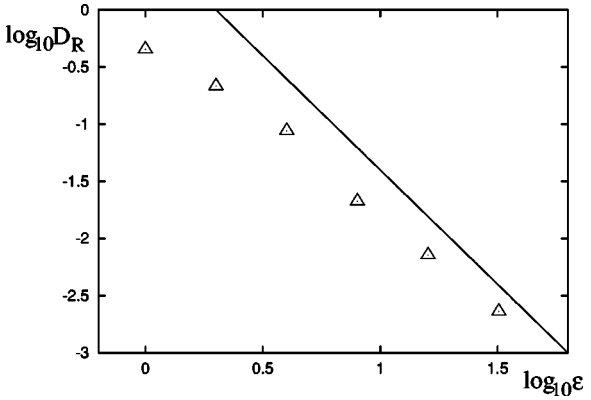

FIG. 11. Numerically measured values of the renormalized diffusion coefficient for larger values of ϵ which lie beyond the perturbative regime, plotted on a log-log scale. The solid line has a slope of -2 and is a guide to the eye, showing the approximate relationship $D_R \sim \epsilon^{-2}$.

The inclusion of V in our original model leads to the following system of equations for the cell positions:

$$\dot{\mathbf{x}}_i = \xi_i + \alpha \nabla_i \phi - \sum_{j \neq i} \nabla_i V(|\mathbf{x}_i - \mathbf{x}_j|), \tag{57}$$

where ϕ still satisfies the diffusion equation (3). In the above equation, the vector $\mathbf{x}_i$ denotes the position of the center of mass of cell i. We have assumed a spherically symmetric

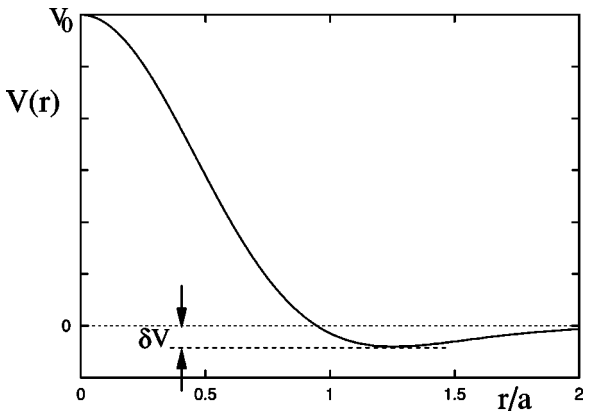

FIG. 12. Schematic of the intercellular potential $V(r)$ showing short-range repulsion and weak attraction, with strength δV over a range of approximately one to two cell diameters a.

potential V identical for all pairs of cells. Naturally, both of these assumptions can be relaxed when necessary. It is even possible for the potential V to have a functional form dictated by the local configuration of neighboring cells. This is an interesting direction to pursue, as it would allow nontrivial cell shape deformations to be modeled in a self-consistent manner.

Much of the foregoing analysis, based on probability distributions and diagrammatics, may be developed to include the potential V. We shall content ourselves here with a brief description of mean-field theory In a similar manner to the derivation of the equation of motion for $P_i(\mathbf{x},t)$ given in Sec. II, we find

$$\partial_t P_i = D_0 \nabla^2 P_i - \varepsilon \nabla \cdot \int d^d x' \int_0^t dt' [\nabla G_\lambda(\mathbf{x}-\mathbf{x}',t-t')] \times \sum_j P_{i,j}(\mathbf{x},t;\mathbf{x}',t') + \nabla \cdot \int d^d x' [\nabla V(|\mathbf{x}-\mathbf{x}'|)] \sum_{j\neq i} P_{i,j}(\mathbf{x},t;\mathbf{x}',t). \quad (58)$$

Applying the mean-field approximation $P_{i,j}=P_iP_j$ and summing the equation over the cell index i we find a self-consistent equation for the cell density $\rho(\mathbf{x},t)$:

$$\partial_t \rho = D_0 \nabla^2 \rho + \nabla \cdot \rho \nabla \int d^d x' \left[V(|\mathbf{x}-\mathbf{x}'|)\rho(\mathbf{x}',t) - \varepsilon \int_0^t dt' G_\lambda(\mathbf{x}-\mathbf{x}',t-t')\rho(\mathbf{x}',t') \right]. \quad (59)$$

Interestingly, this equation, in the absence of the chemotactic term, has been recently introduced within the context of social dynamics, with application to phenomena such as "swarming" [33,34]. Deviations from mean-field theory will be less severe in the absence of long-range chemical interactions, since the nonlinear potential term is local in time. One can show that statistical correlations will not lead to a renormalization of cell diffusion through short-range cell-cell interactions.

IX. DISCUSSION AND CONCLUSIONS

We have introduced and analyzed a stochastic individual-based model of chemotactic cell movement. In this preliminary work, we have focused on a single cell type with a single chemical signaling field, which may be used either for positive (aggregating) or negative (repelling) chemotaxis. As discussed in Sec. II, the model consists of a set of N Langevin equations (1) for the dynamics of the positions of the N cells, along with a continuum diffusion equation for the chemical field (3). This representation allows intuitive model building and the extraction of efficient numerical algorithms. However, for mathematical analysis, it is convenient to describe the dynamics of the system in terms of multicell probability distribution functions (PDF's). The equation of motion for the single-cell PDF P_i [Eq. (9)] contains the two-cell PDF $P_{i,j}$. This is the tip of an infinite hierarchy of multicell PDF's and is typical of interacting many-body systems.

In Sec. III we described a diagrammatic representation of the PDF's. Exact diagrammatic relations were derived for single-cell and two-cell PDF's (Figs. 2 and 3). With the aid of these relations, we derived the diagrammatic perturbation theory for P_i to two loops (i.e., up to and including terms of second order in the chemotactic coupling ϵ). The two-loop diagrams fall into a number of classes, such as tree diagrams, renormalization of the single-cell propagator, and renormalization of the chemotactic coupling. A diagram also arises which lies outside the "dressed" mean-field theory, and which shows single-cell diffusion mediated by two-cell interactions (Fig. 6, diagram n). The hierarchy of PDF's can be broken simply at the first level by imposing $P_{i,j}=P_iP_j$; namely, by discarding statistical correlations between cells. In Sec. IV this mean-field approximation was shown to lead exactly to the deterministic Keller-Segel equations of chemotactic aggregation (22) and (24), which provides a useful benchmark for our model.

In Sec. V we analyzed the stochastic theory exactly within perturbation theory. We concentrated on calculating the renormalization of the cell diffusion coefficient, and presented results to first order in ε for dimensions $d=1$, 2, and 3 [Eq. (35)], and to second order in ϵ for $d=1$ [Eq. (41)]. We restricted our analysis of the second-order effects to $d=1$ since this is the case in which the strongest corrections to mean-field theory are expected. The first-order corrections to D_0 are proportional to $(-\epsilon)$, which is to be expected: e.g., for positive chemotaxis it is intuitive that the cell is attracted somewhat by its own signal and is consequently reduced in its diffusive ability. Interestingly, the second-order corrections are proportional to $(+\epsilon^2)$, the sign remaining positive for all values of the other model parameters. This hints that positive autochemotactic interactions are not strong enough to reduce the renormalized conclusion is borne out from the results of a careful numerical analysis. We stress that the results described above hold when the chemical field has a nonzero decay rate λ. If $\lambda=0$ then the perturbation theory diverges for $t\to\infty$, signaling a different type of dynamics—either autochemotactic collapse or anomalous diffusion. Numerical work on a related discrete model suggests the latter [30]. This case can in principle be studied within a renormalization group calculation, perturbatively about two dimensions.

An alternative closure scheme to mean-field theory, namely, the necklace approximation, was explored in Sec. VI. Although an uncontrolled approximation within the current model, this closure scheme would be appropriate for a specific model in which cells have inhibited ability to relay signals before responding to a prior signal. The necklace approximation leads to an analytically tractable theory for single-cell autochemotactic response. We found that the exact one-loop perturbative result for the diffusion coefficient is exact to all orders within this approximation scheme. It follows that the cell becomes immobile for values of the (positive) chemotactic coupling above a critical value. Precisely at the critical point we showed that the cell wandering is anomalous, with the root-mean-square spatial deviation of

the cell increasing subdiffusively as $t^{1/4}$. These results are applicable in all dimensions, although some doubt is cast on their validity by the nonpositivity of the density at the critical point.

Our main results on the perturbative renormalization of the cell diffusion coefficient due to autochemotactic response were carefully checked by numerical integration of the theory (Sec. VII). Very satisfactory quantitative agreement with the perturbative results was found for small coupling. The strong coupling limit was also explored yielding a smooth decay of the renormalized diffusion coefficient with increasing positive ϵ. The numerical results indicate $D_R \sim \epsilon^{-2}$ for large $\epsilon > 0$. This result is consistent with preliminary calculations from a strong coupling analysis, the details of which will be given elsewhere [32]. Our numerical scheme, derived from the Langevin representation of the model, is "off lattice" and requires knowledge of only the cell positions. The chemical field is not explicitly integrated, and is implemented in the simulations via exact diffusive Green functions. This allows high-speed integration of the model and is ideal for cell simulations in higher dimensions, since the efficiency of the algorithm depends only on the number of cells—not on the dimension of space.

Finally, in Sec. VIII we examined a biological weakness of the original model, that being the treatment of cells as point particles. The finiteness of the cell diameter, along with short-range intercellular adhesion interactions, were shown to be easily incorporated into the Langevin framework via an "effective intercellular potential." We restricted our analysis of this term to mean-field level, within which we showed that our stochastic model becomes equivalent to nonlinear "social dynamics" models that have attracted recent interest such as simple models of swarming [33,34].

Now that we have established this general framework for analyzing statistical correlations in multicellular systems, there are numerous avenues for future research. In the short term we are interested in calculating perturbative renormalization of the chemotactic coupling ϵ, such terms arising from certain two-loop diagrams discussed in Sec. V. It would also be interesting to use perturbative renormalization group methods to calculate the anomalous single-cell distribution function in the case $\lambda = 0$. In terms of strong coupling methods, given the weaknesses of the necklace approximation, it is worthwhile exploring alternative resummation schemes. Along these lines, we have been developing a strong coupling method based on asymptotic analysis of the formal solution to the Langevin equation (53), the results of which will be discussed elsewhere [32]. In the longer term, it is important to make contact with more biological examples. This necessitates more complicated models, but such models can still be constructed using the methods outlined here. Two examples which introduce only modest complications and which may be analytically tractable are (i) aggregation of cells in the presence of two chemical fields: a chemoattractant and a degrading enzyme [3], and (ii) an interacting system of bacterial prey and predating amoeba [2]. For truly complex situations, such as processes occurring in the early embryo, the formalism introduced here is still appropriate, but must be implemented via numerical algorithms. We are hopeful that algorithms based on Eq. (53) will be highly efficient for such tasks as they can be realistically applied to large cell numbers in three dimensions.

In conclusion, we have presented a preliminary analysis of statistical correlations in multicellular systems. Our theoretical framework resembles the many-body theory used to study interacting systems in condensed matter, nuclear physics, and the liquid state. Nontrivial complications in cellular systems stem from memory effects built into the interactions via the diffusing signaling fields. Strongly interacting cell systems abound in nature. Some, such as biofilms [35], are important from the biotechnical and bioengineering perspectives; while others, such as aggregating amoebas (e.g., *Dictyostelium*) [3] and early embryos [8], are central to our understanding of the evolution of organisms and associated fundamental issues of development. Our long-term aim is to use the theory developed in this paper as a framework for the study of these more complex systems. There is no limitation on the number of cell types and signaling fields which may be incorporated into this framework. However, we have shown that even the simplest case of one cell type and one chemical field possesses nontrivial dynamics due to strong statistical correlations. These correlations are a general consequence of motile agents which respond to a complex environment that they, themselves, have produced.

ACKNOWLEDGMENTS

It is a pleasure to thank Alan McKane, Hans Othmer, Kevin Schmidt, and Cornelius Weijer for interesting discussions. T.J.N. also thanks Thomas Hillen and Hans Othmer for encouragement through participation in the SIAM minisymposium "Frontiers in Chemotaxis Modeling." The authors gratefully acknowledge partial support from the NSF (Grant No. DEB-0328267).

APPENDIX A: A GUIDE TO THE DIAGRAMMATIC REPRESENTATION

We give here a brief guide to the use and interpretation of diagrams for those readers who are unfamiliar with this technique. The rationale for employing diagrams is twofold: first, diagrams allow one to gain an intuitive sense of the structure of a theory (since pictures are easier to comprehend than integrals); and second, the logical structure of diagrams enables lengthy calculations to be performed in a far more efficient manner.

In this appendix we will present two of the diagrammatic steps of the paper in detail. This should allow the reader to reconstruct the other numerous diagrammatic manipulations we have used. We also refer the reader to the textbook of Mattuck [24] for a good introduction to the use of diagrams, albeit in the distinct field of condensed matter physics.

Consider the formal solution Eq. (13) to the equation of motion (12) for the probability distribution $\tilde{P}_i(\mathbf{k},t)$, which we repeat below:

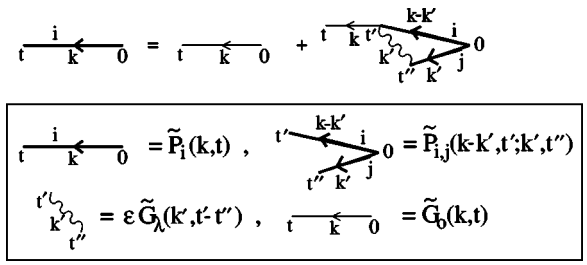

FIG. 13. The diagrammatic representation of Eq. (A1) with explicit labeling of times and wave vectors. An explicit key relating the diagrammatic elements to the underlying propagators and probability distributions is given within the boxed area.

$$\tilde{P}_i(\mathbf{k},t) = \tilde{G}_0(\mathbf{k},t) + \varepsilon \int_0^t dt' \tilde{G}_0(\mathbf{k},t-t') \times \int_0^{t'} dt'' \int dk' (\mathbf{k}\cdot\mathbf{k}') \tilde{G}_\lambda(\mathbf{k}',t'-t'') \times \sum_j \tilde{P}_{i,j}(\mathbf{k}-\mathbf{k}',t';\mathbf{k}',t''). \quad \text{(A1)}$$

We can represent this equation in diagrammatic form by defining a "key" in which the Green functions and probability distributions are written uniquely in terms of diagrammatic elements. This key and the diagrammatic form of Eq. (A1) are given in Fig. 13, where we have labeled each element of the equation in detail. Time flows from right to left within each term of the equation, and wave vectors (whose flow is indicated by the arrows) are conserved at each diagrammatic vertex. All dummy variables are to be integrated over the allowable range; e.g., the variable t' is to be integrated from 0 to t. One must be careful to remember the wave vector weight $(\mathbf{k}\cdot\mathbf{k}')$ at the vertex between the chemical propagator (wavy line) and the outgoing cell diffusion propagator (faint line). Once the diagrammatic rules are familiar it is no longer necessary to explicitly label the equation, and then one draws Fig. 13 in the reduced form given in Sec. III (Fig. 2).

The diagrammatic derivation of the perturbation theory presented in Fig. 6 from the theory encapsulated in Figs. 2, 3, and 5 involves direct substitution of Fig. 3 into Fig. 2, and further substitution of the various combinations from Fig. 5 into the resulting diagrammatic equation. Only the topology of a diagram is relevant, and so although one may find rather "messy" diagrams after the substitutions outlined above, one can redraw such diagrams, carefully preserving their topology, until one finds a systematic (and aesthetically coherent) form. Such a form varies with taste—the authors find the form of the diagrams in Fig. 6 quite satisfactory.

After perturbation theory has been performed using diagrams, one needs to unwrap the diagrams as integrals, so as to mathematically evaluate their contribution. We present here an explicit transcription of the one-loop diagram in Fig. 7, by redrawing this diagram (Fig. 14) in the explicit representation. Given the key in Fig. 13, the transcription should be clear, yielding Eq. (27) in the main text.

APPENDIX B: TWO-LOOP CONTRIBUTIONS TO D_R

There are three two-loop diagrams which contribute to the renormalization of the cell diffusion constant. We summarize here their evaluation. We shall work exclusively in one spatial dimension for the reasons given in Sec. V.

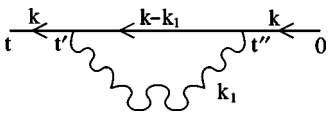

FIG. 14. The one-loop necklace diagram with explicit labeling. Using the key from Fig. 13, the reader will be able to reconstruct Eq. (27).

We write the two-loop correction to $\tilde{G}_R(k,t)$ as

$$\tilde{G}_R^{(2)}(k,t) = \tilde{\Sigma}_1(k,t) + \tilde{\Sigma}_2(k,t) + \tilde{\Sigma}_3(k,t), \quad \text{(B1)}$$

where Σ_n refers to the two-loop diagrams in Fig. 7, which in order, we refer to as the "necklace diagram" $(n=1)$, the "rainbow diagram" $(n=2)$, and the "crossover diagram" $(n=3)$. Likewise, we break the two-loop contribution to D_R into three parts:

$$D_R^{(2)}(k,t) = \Delta_1 + \Delta_2 + \Delta_3, \quad \text{(B2)}$$

where, from Eq. (31), we have

$$\Delta_n = -\frac{1}{2}\lim_{s\to 0} s^2 [\partial_k^2 \hat{\Sigma}_n(k,s)]_{k=0}. \quad \text{(B3)}$$

In terms of the dimensionless coupling $\tilde{\epsilon}=\tilde{\epsilon}(1)$ (36) the coefficient of the two-loop contribution to D_R can be written as [cf. Eq. (41)]

$$F(\delta) = F_1(\delta) + F_2(\delta) + F_3(\delta), \quad \text{(B4)}$$

where we extract the individual contributions via

$$F_n(\delta) = \left(\frac{\varepsilon}{\tilde{\varepsilon}}\right)^2 \frac{\Delta_n}{D_0}. \quad \text{(B5)}$$

We now sketch the computation of these three contributions to $F(\delta)$.

1. The necklace diagram

Laplace transforming in time we have

$$\hat{\Sigma}_1(k,s) = \hat{G}_0(k,s)^3 \int dk_1 \int dk_2 k^2 k_1 k_2 \times [s+\lambda + D_1 k_1^2 + D_0 (k-k_1)^2]^{-1} \times [s+\lambda + D_1 k_2^2 + D_0 (k-k_2)^2]^{-1}. \quad \text{(B6)}$$

No explicit evaluation is necessary due to the explicit factor of k^2. In the limit dictated by Eq. (B3) we find $\Delta_1=0$ and thus $F_1=0$.

2. The rainbow diagram

Laplace transforming in time we have

$$\hat{\Sigma}_2(k,s) = \hat{G}_0(k,s)^2 \int dk_1 \int dk_2 k k_1 k_2 (k-k_2) \times [s+\lambda + D_1 k_2^2 + D_0(k-k_2)^2]^{-2} \times [s+2\lambda + D_1(k_1^2+k_2^2) + D_0(k-k_1-k_2)^2]^{-1}. \tag{B7}$$

The denominators are exponentiated using the integral representation:

$$B^{-\phi} = [\Gamma(\phi)]^{-1} \int_0^\infty da\, a^{\phi-1} e^{-aB}. \tag{B8}$$

This allows the wave vector integrals to be straightforwardly evaluated via completing the square. On differentiating twice with respect to k and taking the limit dictated by Eq. (B3) we find

$$\Delta_2 = \frac{D_0}{8\pi\lambda(D_0+D_1)^3} \int_0^\infty da\, a e^{-a} \int_0^\infty db\, e^{-2b} \times \left[\frac{(2-3\delta)}{b^{1/2}[a+(1-\delta^2)b]^{3/2}} + \frac{3\delta^2(1-\delta)b^{1/2}}{[a+(1-\delta^2)b]^{5/2}} \right], \tag{B9}$$

with δ as given in Eq. (40). The evaluation of this double integral is straightforward but tedious, and gives a contribution to $F(\delta)$ of the form

$$F_2(\delta) = \frac{1}{\pi} \left\{ \frac{(1-\delta)(2\delta^4+\delta^3+6\delta^2+\delta-2)}{(1-\delta^2)^{1/2}(1+\delta^2)^2} + \frac{2(2-3\delta-\delta^2)}{(1+\delta^2)^{5/2}} \sin^{-1}\left(\frac{1+\delta^2}{2} \right)^{1/2} \right\}. \tag{B10}$$

3. The crossover diagram

Laplace transforming in time we have

$$\hat{\Sigma}_3(k,s) = \hat{G}_0(k,s)^2 \int dk_1 \int dk_2\, k k_1\, k_2 (k-k_2) \times [s+\lambda + D_1 k_1^2 + D_0(k-k_1)^2]^{-1} \times [s+\lambda + D_1 k_2^2 + D_0(k-k_2)^2]^{-1} \times [s+2\lambda + D_1(k_1^2+k_2^2) + D_0(k-k_1-k_2)^2]^{-1}. \tag{B11}$$

As for the rainbow diagram, the denominators are exponentiated using the integral representation (B8) which allows the wave vector integrals to be straightforwardly evaluated. On differentiating twice with respect to k and taking the limit dictated by Eq. (B3) we find

$$\Delta_3 = \frac{D_0}{8\pi\lambda(D_0+D_1)^3} \int_0^\infty da\, e^{-a} \int_0^\infty db\, e^{-b} \int_0^\infty dc\, e^{-2c} \times \left[\frac{a+2c}{[(a+c)(b+c)-\delta^2 c^2]^{3/2}} - \frac{3\delta c(a+c)(b+(1-\delta)c)}{[(a+c)(b+c)-\delta^2 c^2]^{5/2}} \right]. \tag{B12}$$

The evaluation of this triple integral is straightforward but tedious, and gives a contribution to $F(\delta)$ of the form

$$F_3(\delta) = \frac{1}{\pi} \left\{ \frac{(1-\delta)^2}{(1-\delta^2)^{1/2}(1+\delta^2)} + \frac{2\delta}{(1+\delta^2)^{3/2}} \sin^{-1}\left(\frac{1+\delta^2}{2} \right)^{1/2} + \frac{\pi(1-\delta)}{2\delta^2} \left[\frac{4}{\pi(1+\delta^2)^{1/2}} \sin^{-1}\left(\frac{1+\delta^2}{2} \right)^{1/2} - 1 \right] \right\}. \tag{B13}$$

The forms of F_n $(n=1,2,3)$ along with their sum $F(\delta)$ are plotted in Fig. 8 in the main text. It is interesting to note that for δ close to unity the contributions from the rainbow and crossover diagrams have different signs, but conspire to give a sum which is positive, albeit vanishingly small in the limit $\delta \to 1$.

[1] B. Alberts, A. Johnson, J. Lewis, M. Raff, K. Roberts, and P. Walter, *Molecular Biology of the Cell*, 4th ed. (Garland, New York, 2002).

[2] J. P. Armitage and J. M. Lackie, *Biology of the Chemotactic Response* (Cambridge University Press, Cambridge, U.K., 1990).

[3] R. H. Kessin, *Dictystelium: Evolution, Cell Biology, and the Development of Multicellularity* (Cambridge University Press, Cambridge, U.K., 2001).

[4] E. F. Keller and L. A. Segel, J. Theor. Biol. **26**, 399 (1970).

[5] E. F. Keller and L. A. Segel, J. Theor. Biol. **30**, 225 (1971).

[6] H. Othmer and A. Stevens, SIAM (Soc. Ind. Appl. Math.) J. Appl. Math. **57**, 1044 (1997).

[7] T. Hillen and K. Painter, Adv. Appl. Math. **26**, 280 (2001).

[8] L. Wolpert, R. Beddington, T. Jessell, P. Lawrence, E. Meyerowitz, and J. Smith, *Principles of Development*, 2nd ed. (Oxford University Press, Oxford, 2002).

[9] R. Bellairs and M. Osmond, *An Atlas of Chick Development* (Academic, London, 1998).

[10] G. C. Schoenwolf, *Laboratory Studies of Vertebrate and Invertebrate Embryos* (Prentice-Hall, Englewood Cliffs, NJ, 2001).

[11] R. T. Tranquillo, D. A. Lauffenberger, and S. H. Zigmond, J. Cell Biol. **106**, 303 (1988).

[12] M. Eisenbach, Rev. Reprod. **4**, 56 (1999).

[13] L. Kadanoff, *Statistical Physics: Statics, Dynamics, and Renormalization* (World Scientific, Hackensack, NJ, 2000).

[14] D. Drasdo, R. Kree, and J. S. McCaskill, Phys. Rev. E **52**, 6635 (1995).

[15] D. Drasdo, Phys. Rev. Lett. **84**, 4244 (2000).

[16] D. Drasdo and G. Forgacs, Dev. Dyn. **219**, 182 (2000).

[17] J. A. Glazier and F. Graner, Phys. Rev. E **47**, 2128 (1993).

[18] F. Graner and J. A. Glazier, Phys. Rev. Lett. **69**, 2013 (1993).

[19] M. Zajac, G. L. Jones, and J. A. Glazier, J. Theor. Biol. **222**, 247 (2003).
[20] C. W. Gardiner, *Handbook of Stochastic Methods*, 2nd ed. (Springer, Berlin, 1995).
[21] A. Stevens, SIAM (Soc. Ind. Appl. Math.) J. Appl. Math. **61**, 183 (2000).
[22] E. M. Lifshitz and L. P. Pitaevskii, *Physical Kinetics* (Pergamon, Oxford, 1993).
[23] E. M. Lifshitz and L. P. Pitaevskii, *Statistical Physics Part 2* (Pergamon, Oxford, 1989).
[24] R. D. Mattuck, *A Guide to Feynman Diagrams in the Many-body Problem*, 2nd ed. (Dover, New York, 1992).
[25] *Handbook of Mathematical Functions*, edited by M. Abramowitz and I. A. Stegun (Dover, New York, 1972).
[26] S.-K. Ma, *Modern Theory of Critical Phenomena* (Benjamin, Reading, MA, 1976).
[27] T. Tsuneto and E. Abrahams, Phys. Rev. Lett. **30**, 217 (1973).
[28] G. 't Hooft, Nucl. Phys. B **72**, 461 (1974).
[29] M. A. Fisher, J. Stat. Phys. **34**, 667 (1984).
[30] S. Sa-nguansin, R. Grima, and T. J. Newman (unpublished).
[31] R. Grima and T. J. Newman, Phys. Rev. E **70**, 036703 (2004).
[32] R. Grima and T. J. Newman (unpublished).
[33] G. Flierl, D. Grunbaum, and S. Levin, J. Theor. Biol. **196**, 397 (1999).
[34] A. Mogilner, L. Edelstein-Keshet, L. Bent, and A. Spiros, J. Math. Biol. **47**, 353 (2003).
[35] L. Hall-Stoodley, J. W. Costerton, and P. Stoodley, Nat. Rev. Microbiol. **2**, 95 (2004).